The Astrophysical Journal Letters, 980:L30 (9pp), 2025 February 20 https://doi.org/10.3847/2041-8213/adb151

Signatures of Rapidly Rotating Stars with Chemically Homogeneous Evolution in the First Galaxies

Boyuan Liu[1], Yves Sibony[2], Georges Meynet[2], and Volker Bromm[3,4]
[1] Institut für Theoretische Astrophysik, Zentrum für Astronomie, Universität Heidelberg, D-69120 Heidelberg, Germany; boyuan.liu@uni-heidelberg.de
[2] Department of Astronomy, University of Geneva, Chemin Pegasi 51, 1290 Versoix, Switzerland
[3] Department of Astronomy, University of Texas at Austin, 2515 Speedway, Stop C1400, Austin, TX 78712, USA
[4] Weinberg Institute for Theoretical Physics, University of Texas at Austin, Austin, TX 78712, USA
Received 2024 December 3; revised 2025 January 12; accepted 2025 February 2; published 2025 February 14

Abstract

The James Webb Space Telescope (JWST) has revealed an unexpectedly high abundance of UV luminous galaxies at redshifts $z \gtrsim 10$, challenging "standard" galaxy formation models. This study investigates the role of rapidly rotating (massive) stars undergoing chemically homogeneous evolution (CHE) in reconciling this potential tension. These stars are more compact, hotter, and exhibit enhanced UV emission. We find that the rest-frame UV luminosity of star-forming galaxies can be significantly enhanced by a factor of $\sim$3−6 when CHE stars above a minimum initial mass of $m_{\star,\min}^{\rm CHE} \sim 2$–$10\,M_{\odot}$ account for more than half of the total stellar mass following a Salpeter initial mass function. As a result, the UV luminosity functions observed at $z \sim 12-16$ can be reproduced with less extreme values of star formation efficiency and UV luminosity stochastic variability. Our results highlight the potential of CHE in explaining the UV-bright galaxy populations detected by JWST and call for future work to explore the broader astrophysical implications of CHE and its associated phenomena in the early universe, such as gamma-ray bursts, compact object binaries, and metal enrichment.

Unified Astronomy Thesaurus concepts: High-redshift galaxies (734); Population III stars (1285); Population II stars (1284); James Webb Space Telescope (2291); Early universe (435); Stellar evolution (1599)

1. Introduction

Early results from the James Webb Space Telescope (JWST) have challenged the standard model of galaxy formation in the high-z universe (M. Boylan-Kolchin 2023), with the discovery of a surprising abundance of UV-bright galaxies at $z \gtrsim 10$ (e.g., C. T. Donnan et al. 2023, 2024; S. L. Finkelstein et al. 2023, 2024; Y. Harikane et al. 2023; I. Labbé et al. 2023; N. J. Adams et al. 2024). Two broad classes of explanations have been discussed: modifications to the underlying ΛCDM model of cosmological structure formation (e.g., B. Liu & V. Bromm 2022; X. Shen et al. 2024) or models that vary assumptions in the standard picture of star formation. The second (baryonic) category explores scenarios that either increase the stellar mass/star formation rate (SFR) in a given dark matter host halo, by boosting the star formation efficiency (SFE, e.g., K. Inayoshi et al. 2022; A. Dekel et al. 2023) or variability/burstiness of UV emission/star formation (e.g., X. Shen et al. 2023), or those that enhance the stellar light-to-mass ratio (e.g., C. T. Donnan et al. 2025). An example for the latter explores a top-heavy initial mass function (IMF; e.g., K. Inayoshi et al. 2022; E. R. Cueto et al. 2024; A. Trinca et al. 2024; E. M. Ventura et al. 2024), as predicted for the metal-poor environments in the early universe (e.g., B. Liu et al. 2024). UV emission can also be enhanced when strong radiation-pressure-driven outflows remove UV dust attenuation during the early evolution of high-z galaxies (e.g., A. Ferrara 2024).

Invoking a top-heavy IMF or an increased formation efficiency may, however, only boost star formation locally, but suppress it on galactic scales, by triggering disruptive stellar feedback, such as strong supernova (SN) activity (e.g., T. B. Jeong et al. 2024). Here we propose a different (baryonic) solution for the early UV-bright galaxy problem: the stellar light-to-mass ratio is boosted because of a population of stars that undergo chemically homogeneous evolution (CHE), which become more compact and hotter than stars without CHE.[5] Such a CHE stage could be realized for rapidly rotating stars, where their structure adapts by triggering strong internal mixing currents (e.g., A. Maeder 1987; S. C. Yoon & N. Langer 2005; M. Cantiello et al. 2007; J. J. Eldridge et al. 2011; J. J. Eldridge & E. R. Stanway 2012, 2016; A. Maeder & G. Meynet 2012; S. C. Yoon et al. 2012; D. Szécsi et al. 2015, 2022; S. E. de Mink & I. Mandel 2016; I. Mandel & S. E. de Mink 2016; H. F. Song et al. 2016; P. Marchant et al. 2017; D. R. Aguilera-Dena et al. 2018; Z. Cui et al. 2018; B. Kubátová et al. 2019; L. du Buisson et al. 2020; J. Riley et al. 2021; S. Ghodla et al. 2023; A. Dorozsmai et al. 2024). Rotation speeds close to the break-up value have been predicted for the first Population III (Pop III) stars, formed in the unique metal-free conditions[6] of dark matter minihalos (A. Stacy et al. 2011, 2013). Similarly, metal-poor Population II (Pop II) stars may be able to retain their natal rotation speeds because of their significantly reduced mass loss due to weakened radiatively driven stellar winds (e.g., J. S. Vink et al. 2001). Recent direct observations of select O-type stars in nearby metal-poor dwarf galaxies suggest that stellar winds may be even weaker than what was previously predicted by theory (A. A. C. Sander et al. 2017, 2018; A. C. Gormaz-Matamala et al. 2024; O. G. Telford et al. 2024).

[5] Similar but weaker effects can also be achieved by initial helium enhancement (H. Katz et al. 2024).
[6] Magnetic fields arising from dynamo activity in the primordial protostellar disks could complicate the situation, leading to a possible bifurcation into cases of rapid and slow rotation (S. Hirano & V. Bromm 2018).

The impact of a CHE boost in the ionizing radiation of H, He, and possibly He^+ from Pop III stars on the early stages of reionization was explored in a previous study (Y. Sibony et al. 2022), placing constraints on the fraction of Pop III stars that undergo CHE (see also e.g., S. Ghodla et al. 2023 and B. Liu et al. 2025, in preparation). The reionization modeling, however, is subject to the uncertain escape fraction of ionizing radiation from the galaxy host halos, whereas any constraints from the nonionizing UV continuum are more direct indications of the underlying stellar populations. We note that there have been recent indications for the metal enrichment from rapidly rotating stars in the first galaxies, inferred from their chemical abundance patterns with deep JWST spectroscopy. Prominent among them are high nitrogen-to-oxygen abundance ratios, e.g., in GN-z11 and RXCJ2248-ID (A. J. Bunker et al. 2023; M. W. Topping et al. 2024), which may be explained with models of rapidly rotating, massive stars (e.g., D. Nandal et al. 2024; S. Tsiatsiou et al. 2024). Another nucleosynthetic signature of rapidly rotating stars is the proposed boost in carbon production (B. Liu et al. 2021; S. K. Jeena et al. 2023), providing a possible explanation for strong carbon emission lines detected in $z \gtrsim 12$ galaxies (e.g., F. D'Eugenio et al. 2024) and carbon-enhanced extremely metal-poor stars in the Milky Way (e.g., J. Zepeda et al. 2023). As the extreme outcome of rotational mixing, CHE leads to the maximal enhancement of carbon production (S. K. Jeena et al. 2023), although it is unclear whether nitrogen enhancement can be achieved by stars with CHE, which presumably depends on how the CHE phase starts and ends. We will therefore explore in the following whether a rapidly rotating subset of stars under CHE within the first galaxies can account for the emerging JWST phenomenology of UV-bright galaxies in the first few hundred million years of cosmic history.

2. CHE

2.1. Stellar Evolution

The stellar evolution models for stars evolving homogeneously are based on $n = 3$ polytropes with a time-varying mass fraction of hydrogen, as detailed in Y. Sibony et al. (2022). In that work Pop III stars with initial masses ($m_\star$) between 9 and 300 $M_\odot$ were computed. Here we complement our previous grid by adding tracks for lower initial mass stars with masses between 1.7 and 7 $M_\odot$. As a comparison sample, we use the stellar tracks for nonrotating Pop III stars in the same mass range (1.7−300 $M_\odot$) from L. J. Murphy et al. (2021). Here, we only consider initially metal-free stellar evolution models for simplicity while freely varying the IMF parameters (see Section 2.2 below). We focus on the main-sequence (MS) phase where most UV photons are produced and ignore mass loss from stellar winds, which is minor for metal-poor stars (e.g., R. Hainich et al. 2015; B. Kubátová et al. 2019). For metal-rich massive stars where winds are strong, the UV emission will be overestimated in our models. This renders our results as optimistic estimates. In fact, for nonrotating stars, the difference in rest-frame UV ($\lambda \sim 1500$ Å) luminosity made by changing the initial metallicity from $Z = 0$ to $Z = 0.02$ under a fixed P. Kroupa (2001) IMF is small (within a factor of $\sim$2) for a typical star formation timescale $\sim$ 100 Myr, according to the Yggdrasil stellar population synthesis models (E. Zackrisson et al. 2011). For CHE stars, B. Kubátová et al. (2019) found that changing the wind parameters (mass loss rate and clumping factor) has negligible effects on the UV spectrum around $\lambda \sim 1000-3000$ Å during MS with helium mass fractions $Y \lesssim 0.98$ for $m_\star \sim 20-130\,M_\odot$ in the metal-poor regime ($Z = 0.0002$), although the impact of winds can be stronger at higher metallicities. However, the impact is expected to be smaller than the case of nonrotating stars since the strong surface enhancement of helium is the dominant factor in CHE, as implied by the smaller effects of metallicity on the properties of pure helium stars (see, e.g., Figures 5 and 6 in G. Iorio et al. 2023).

Homogeneous evolution requires that the timescale for chemical mixing is much smaller than the nuclear timescale during the MS phase. The mixing timescale scales as $R^2/D_{\rm mix}$, where R is the stellar radius and $D_{\rm mix}$ the diffusion coefficient describing the transport of the chemical elements. A. Maeder & G. Meynet (2000, see their paragraph 3.1) showed that the ratio of the mixing timescale to MS lifetime approximately varies as $1/m_\star$ for stars more massive than 15 $M_\odot$. This indicates that when the mass decreases, the mixing timescale increases faster than the MS lifetime. Thus, we can expect to reach a lower initial mass limit, $m_{\star,\rm min}^{\rm CHE}$, below which homogeneous evolution will not be obtained. The precise limit depends on the initial rotation and metallicity, with lower values when the initial rotation increases and when the metallicity decreases (see, e.g., Figure 4 in I. Brott et al. 2011), which is due at least in part to the fact that at lower metallicities, stars are more compact.

This limit also depends on the physics used for chemical mixing and for the transport of angular momentum. These two transport mechanisms are intimately related since the gradients of chemical composition impact angular momentum transfer, which in turn influences the transport of the chemical elements. For this work, since we do not use a peculiar physical mechanism to obtain the homogeneous tracks, we simply consider the value of this limit as a free parameter. Most of the stellar models computed so far have focused on the massive stellar mass range down to lower masses between 4 and 10 $M_\odot$ (see, e.g., S. C. Yoon et al. 2006; I. Brott et al. 2011; D. Szécsi et al. 2015; J. Riley et al. 2021), so we may wonder if it is justified here to extend this limit further. As indicated above, the limit depends on the physics of mixing, which is still not yet fully understood. On the other hand, fast rotation is likely not the only process that may lead to homogeneous stars. For instance, grazing collisions have been found to result in nearly completely mixed stars producing blue stragglers, as observed in globular clusters (e.g., W. Benz & J. G. Hills 1987).

2.2. UV Emission and Stellar Populations

As in Y. Sibony et al. (2022), we consider stars to radiate as blackbodies and compute their average spectral luminosity $L_{\star,\nu}(t, m_\star)$ in a 100 Å window around the typical rest-frame UV wavelength of 1500 Å along their evolutionary tracks. We have verified using detailed stellar atmosphere models computed by the code TLUSTY (I. Hubeny 1988; I. Hubeny et al. 2021) that the relative errors in $L_{\star,\nu}(t, m_\star)$ introduced by the blackbody assumption are within 30% for most CHE and nonrotating stars with $m_\star \sim 3-300\,M_\odot$, surface gravities $g \sim 10^{4.1-5.1}$ cm s^{-2}, and effective temperatures $T_{\rm eff} \sim 10^{4.3}-10^5$ K, which dominate the overall rest-frame UV emission. We also compare our results with those from B. Kubátová et al. (2019) for CHE stars with $Z = 0.0002$ and $m_\star \sim 20-130\,M_\odot$, whose spectra are calculated using the atmosphere code POWR (e.g., A. Sander et al. 2015) from the evolutionary tracks computed by D. Szécsi et al. (2015). The discrepancy is also within 30%

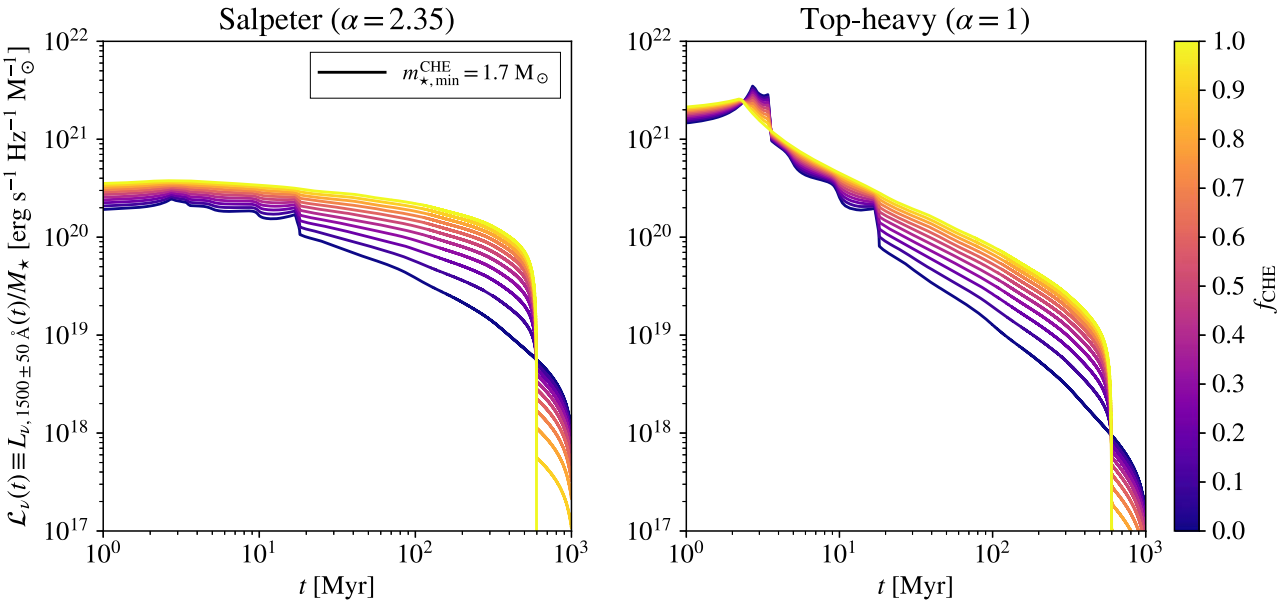

Figure 1. Rest-frame UV light curve: evolution of UV luminosity normalized by the total stellar mass for a single-age stellar population. The left (right) panel shows the results for a Salpeter (top-heavy) IMF, $dN/dm_\star \propto m_\star^{-\alpha}$, with a slope $\alpha = 2.35$ (1) and a mass range $m_\star \in [1.7, 300]\ M_\odot$ for both nonrotating and CHE stars. The mass fraction of CHE stars $f_{\rm CHE}$ is varied between 0 and 1, with lighter colors denoting larger $f_{\rm CHE}$.

during MS ($Y \lesssim 0.98$), mainly resulting from the different evolutionary tracks. When $T_{\rm eff}$ is controlled, the difference caused by the blackbody assumption alone is within 7%. It is shown below that our conclusions are robust despite these uncertainties.

We consider a mixed stellar population containing both CHE and nonrotating stars as a single-age starburst. This population is defined by two parameters: the mass fraction $f_{\rm CHE} \in [0, 1]$ of CHE stars and the minimal stellar mass $m^{\rm CHE}_{\star,\rm min} \in [1.7, 20]\ M_\odot$ for CHE to occur. For a given choice of $(f_{\rm CHE}, m^{\rm CHE}_{\star,\rm min})$, we first generate two stellar populations following a power-law IMF, $dN/dm_\star \propto m_\star^{-\alpha}$, with a slope of $\alpha = 2.35$ (E. E. Salpeter 1955) or $\alpha = 1$ (top-heavy). The population of CHE stars is generated between $m^{\rm CHE}_{\star,\rm min}$ and $m_{\star,\rm max} = 300\ M_\odot$, while nonrotating stars span a fixed mass range from $m_{\star,\rm min} = 1.7\ M_\odot$ to $m_{\star,\rm max} = 300\ M_\odot$. For each population, we compute the total luminosity $L_\nu(t)$ by summing up the $L_{\star,\nu}(t, m_\star)$ for all stars that are still alive at time t, up to $t = 1$ Gyr, which is then normalized by the total initial stellar mass $M_\star$ as $\mathcal{L}_\nu(t) \equiv L_\nu(t)/M_\star$. Finally, we combine the CHE and nonrotating populations so that the mass fraction of CHE stars is $f_{\rm CHE}$. For illustration, Figure 1 shows the resulting rest-frame UV light curves for $m^{\rm CHE}_{\star,\rm min} = 1.7\ M_\odot$ and varying $f_{\rm CHE}$.

Note that in the aforementioned default model, the overall IMF of the mixed population is no longer a strict power law when $f_{\rm CHE} > 0$ and $m^{\rm CHE}_{\star,\rm min} > m_{\star,\rm min} = 1.7\ M_\odot$ as the CHE component is more top heavy than the nonrotating component. An alternative approach is to turn a fraction of the stars above $m^{\rm CHE}_{\star,\rm min}$ into CHE stars while keeping the overall IMF fixed to the chosen power-law form. In this case, the mass fraction of CHE stars has an upper limit $f^{\rm max}_{\rm CHE} = [\int_{m^{\rm CHE}_{\star,\rm min}}^{m_{\star,\rm max}} m_\star (dN/dm_\star) dm_\star]/[\int_{m_{\star,\rm min}}^{m_{\star,\rm max}} m_\star (dN/dm_\star) dm_\star]$ as a function of $m^{\rm CHE}_{\star,\rm min}$. Although we do not model this case explicitly, its outcomes can be estimated from the results of the default model via $f^{\rm max}_{\rm CHE}$, which do not change our conclusions made with the default model.

3. Impact on First Galaxy UV Emission

To predict the UV magnitudes of high-z galaxies and make direct comparisons with observations, we focus on the UV emission efficiency $\eta_{\rm UV} \equiv \kappa_{\rm UV}^{-1}$ defined as the inverse of the conversion factor $\kappa_{\rm UV}$ between SFR and rest-frame UV luminosity L_ν(UV):

$$\mathrm{SFR}/(M_\odot\ \mathrm{yr}^{-1}) = \kappa_{\rm UV} L_\nu(\mathrm{UV})/(\mathrm{erg\ s^{-1}\ Hz^{-1}})\,. \quad (1)$$

A reference value from local calibrations adopted by P. Madau & M. Dickinson (2014) is $\eta_{\rm UV} \simeq 8.70 \times 10^{27}$, corresponding to $\kappa_{\rm UV} = 1.15 \times 10^{-28}$. Given the single-age starburst results (see Figure 1), we calculate $\eta_{\rm UV}$ as a function of the CHE fraction $f_{\rm CHE}$ and minimum mass $m^{\rm CHE}_{\star,\rm min}$ under different IMFs by integrating the stellar mass-normalized light curve $\mathcal{L}_\nu(t)$ over a simple top-hat star formation history with a constant SFR for a period of $t_{\rm SF}$:

$$\eta_{\rm UV} = \int_0^{t_{\rm SF}} \mathcal{L}_\nu(t) dt \times M_\odot\ \mathrm{yr}^{-1}/(\mathrm{erg\ s^{-1}\ Hz^{-1}}). \quad (2)$$

We adopt $t_{\rm SF} = 100$ Myr by default (see Appendix A for the results for $t_{\rm SF} = 10$ and 1000 Myr) as the typical timescale of star formation probed by rest-frame UV emission, which is also close to the halo dynamical timescale and baryon cycle timescale at $z \sim 10$ (e.g., D. Anglés-Alcázar et al. 2017; S. Tacchella et al. 2020; J. A. Flores Velázquez et al. 2021). We have ignored the contribution of nebular emission and dust attenuation. As discussed in Appendix B, for moderately metal-enriched ($Z \gtrsim 0.0004$) luminous high-z galaxies observable by JWST, the enhancement of rest-frame UV emission by CHE with $t_{\rm SF} \gtrsim 10$ Myr can be underestimated by up to a factor of $\sim$2 in the absence of nebular emission, which is also expected to be enhanced for CHE stars due to their strong ionizing power (B. Kubátová et al. 2019; Y. Sibony et al. 2022), and the effect is stronger for more metal-poor systems (E. Zackrisson et al. 2011). Therefore, our results without nebular contributions should be regarded as conservative estimates. The

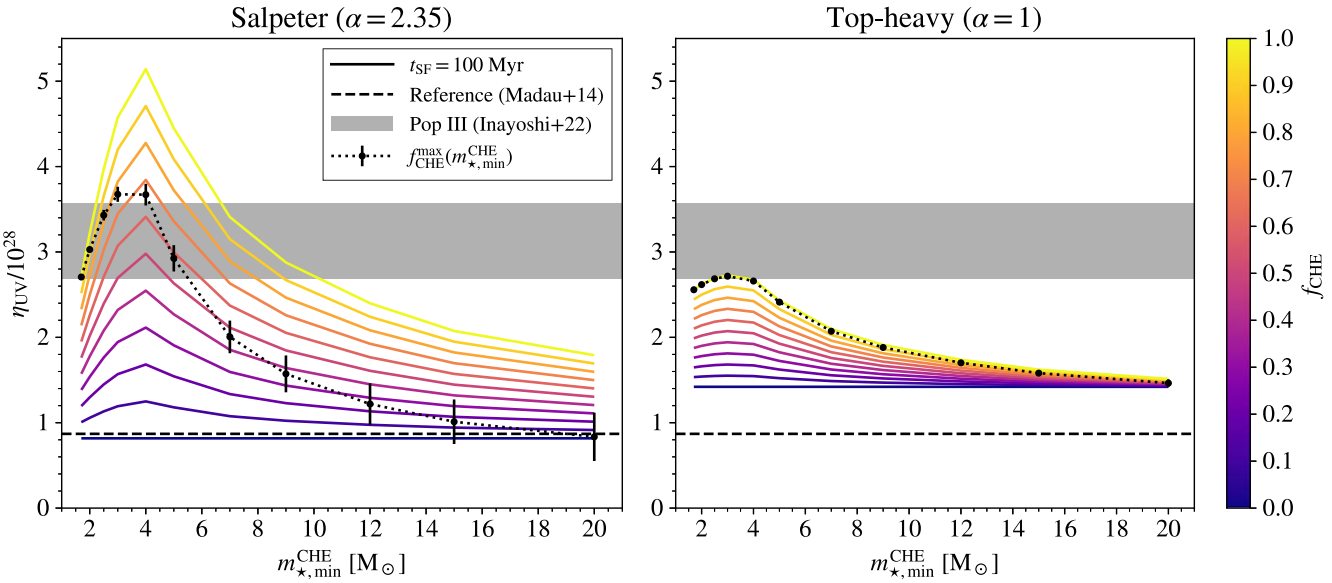

Figure 2. Rest-frame UV luminosity per unit SFR $\eta_{\rm UV}$ for a top-hat star formation history within a timescale $t_{\rm SF} = 100$ Myr. As in Figure 1, the left and right panels show the results for Salpeter and top-heavy IMFs, with $\alpha = 2.35$ and 1, respectively. While the mass range of nonrotating stars is fixed as $m_\star \in [1.7, 300]\ M_\odot$, we plot $\eta_{\rm UV}$ as a function of $m_{\star,\rm min}^{\rm CHE}$ for $f_{\rm CHE} \in [0, 1]$, where $f_{\rm CHE}$ increases for lighter colors (from bottom to top). The dotted curve with error bars shows the maximum $\eta_{\rm UV}$ in the alternative population model with a fixed overall IMF (corresponding to the maximum CHE mass fraction $f_{\rm CHE}^{\rm max}$), which is estimated to be in between $\eta_{\rm UV}(f_{\rm CHE} = f_{\rm CHE}^{\rm max})$ and $f_{\rm CHE}^{\rm max}\,\eta_{\rm UV}(f_{\rm CHE} = 1)$. We also show the reference value $\eta_{\rm UV} \simeq 8.70 \times 10^{27}$ from P. Madau & M. Dickinson (2014) with the dashed line, which is very close to our result for $f_{\rm CHE} = 0$ given $\alpha = 2.35$. The shaded regions show the results for Pop III stars with extremely top-heavy IMFs from K. Inayoshi et al. (2022).

effect of dust attenuation can be effectively absorbed into the UV variability parameter (see below and X. Shen et al. 2023).

The results are shown in Figure 2. We obtain $\eta_{\rm UV} \simeq 8.17 \times 10^{27}$ in the canonical case of Salpeter IMF without CHE ($f_{\rm CHE} = 0$), which is very close to the reference value $\eta_{\rm UV} \simeq 8.70 \times 10^{27}$ (P. Madau & M. Dickinson 2014). This further justifies our choice of $t_{\rm SF} = 100$ Myr (as well as $m_{\star,\rm min} = 1.7\ M_\odot$). Interestingly, the enhancement of UV emission by CHE peaks at $m_{\star,\rm min}^{\rm CHE} = 4$ (3) $M_\odot$ for the Salpeter (top-heavy) IMF, reaching $\eta_{\rm UV} \sim 5.14(2.73) \times 10^{28}$ for $f_{\rm CHE} = 1$, which is higher than the reference value by a factor of $\sim$6 (3). Here, $\eta_{\rm UV}$ does not increase monotonically with $m_{\star,\rm min}^{\rm CHE}$ because the (lifetime-integrated) rest-frame UV emission of CHE stars has a peak around $m_\star \sim 2\,M_\odot$ and decreases for more massive stars, dropping even below the values for nonrotating stars at $m_\star \gtrsim 100\,M_\odot$. Here, massive stars become too hot under CHE, producing primarily more energetic (ionizing) photons (Y. Sibony et al. 2022; B. Liu et al. 2025, in preparation). For the same reason, the effect of CHE is generally stronger at $m_{\star,\rm min}^{\rm CHE} \lesssim 10\,M_\odot$ when α or $t_{\rm SF}$ increase (see Appendix A) or with a smaller IMF upper mass limit $m_{\star,\rm max}$. Without CHE, we obtain $\eta_{\rm UV} = 1.42 \times 10^{28}$ under our top-heavy IMF (that extends down to $m_{\star,\rm min} = 1.7\,M_\odot$ with $\alpha = 1$), moderately increased by $\sim$74 (63)% compared with the Salpeter (reference) case. It is shown in K. Inayoshi et al. (2022, see their Table 1) that considering extremely top-heavy IMFs ($m_\star \gtrsim 10\,M_\odot$) for Pop III stars further increases the UV emission efficiency to $\eta_{\rm UV} \sim 2.68$–3.57×10^{28} (see also V. Bromm et al. 2001). Comparable and higher values of $\eta_{\rm UV}$ can be achieved by CHE with $f_{\rm CHE} \gtrsim 0.5$ and $m_{\star,\rm min}^{\rm CHE} \sim 2$–$10\,M_\odot$ under a Salpeter IMF.

Given the results of $\eta_{\rm UV}(f_{\rm CHE})$ in the default model, the maximum UV efficiency in the alternative case of a fixed overall IMF should be in between $\eta_{\rm UV}(f_{\rm CHE} = f_{\rm CHE}^{\rm max})$ (with optimistic contributions from nonrotating stars below $m_{\star,\rm min}^{\rm CHE}$) and $f_{\rm CHE}^{\rm max}\,\eta_{\rm UV}(f_{\rm CHE} = 1)$ (ignoring nonrotating stars below $m_{\star,\rm min}^{\rm CHE}$). The resulting values are very close to $\eta_{\rm UV}(f_{\rm CHE} = 1)$ for the top-heavy IMF ($\alpha = 1$) as $f_{\rm CHE}^{\rm max} > 0.94$. For the Salpeter IMF with $f_{\rm CHE}^{\rm max} \sim 0.3$–1, the maximum UV emission efficiency peaks around $m_{\star,\rm min}^{\rm CHE} \sim 3$–$4\,M_\odot$ given $f_{\rm CHE}^{\rm max} \sim 0.7$–0.8, reaching $\eta_{\rm UV} \sim 3.6$–3.8×10^{28}, which is still a factor of $\sim$4 larger than the reference value.

Once $\eta_{\rm UV}$ is known, we derive the UV luminosity function (UVLF) using the model in X. Shen et al. (2023). First, we calculate the median UV magnitude $M_{\rm UV}$ as a function of halo mass $M_{\rm h}$ from the median SFR $= \epsilon_\star f_{\rm b} \dot{M}_{\rm h}$ estimated by the median halo accretion rate (O. Fakhouri et al. 2010),

$$\dot{M}_{\rm h} \simeq 25.3\ M_\odot\ {\rm yr}^{-1} \left(\frac{M_{\rm h}}{10^{12} M_\odot}\right)^{1.1} \times (1 + 1.65z)\sqrt{\Omega_{\rm m}(1+z)^3 + \Omega_\Lambda}, \quad (3)$$

and SFE (e.g., S. Tacchella et al. 2018; Y. Harikane et al. 2023),

$$\epsilon_\star = \frac{2\epsilon_0}{(M_{\rm h}/M_0)^{-\gamma} + (M_{\rm h}/M_0)^{\xi}}. \quad (4)$$

Here $f_{\rm b} \equiv \Omega_{\rm b}/\Omega_{\rm m} \simeq 0.16$ is the cosmic baryon fraction, and we adopt $\epsilon_0 = 0.1$, $\gamma = 0.6$, and $\xi = 0.5$ based on P. Behroozi et al. (2019) for the normalization and low-mass slope, matching the SFR–$M_{\rm h}$ relation at $z = 7$ and Y. Harikane et al. (2023) for the high-mass slope. Next, this median $M_{\rm UV}$–$M_{\rm h}$ relation is combined with the halo mass function[7] $dn/d\log M_{\rm h}$ to derive the *median* UVLF $dn_{\rm median}/dM_{\rm UV} = (dn/d\log M_{\rm h})|\frac{d\log M_{\rm h}}{dM_{\rm UV}}|$, which is then

[7] We use the HMF package (S. G. Murray et al. 2013) to calculate the halo mass function with the J. L. Tinker et al. (2010) model and real-space top-hat window function for a flat ΛCDM cosmology. The relevant cosmological parameters are based on Planck Collaboration et al. (2020) results: $H_0 = 67.66$ km s^{-1} Mpc^{-1}, $\Omega_{\rm m} = 0.30966$, $n_{\rm s} = 0.9667$, $\sigma_8 = 0.8159$, and $\Omega_{\rm b} = 0.04897$.

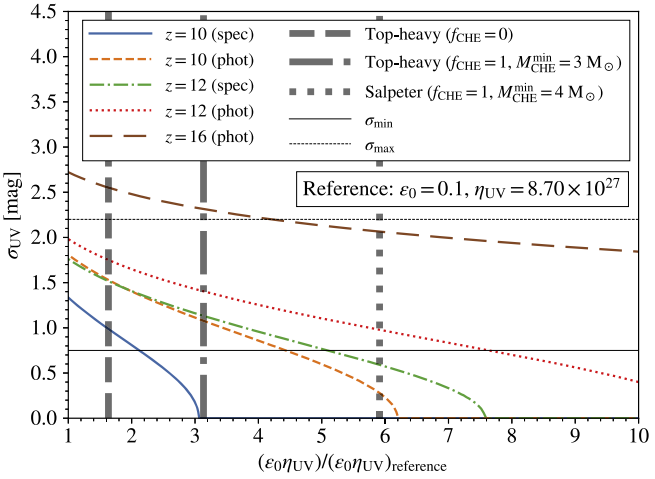

Figure 3. Constraints on UV emission efficiency and variability from JWST data. The colored curves show the values of $\epsilon_0\eta_{\rm UV}$ and $\sigma_{\rm UV}$ required to reproduce $\log(\Phi(M_{\rm UV}=-20.5)\,[{\rm mag}^{-1}\,{\rm cMpc}^{-3}])=-5$ and -5.3 at $z=10$ (solid) and 12 (dashed–dotted) based on spectroscopy and $\log(\Phi(M_{\rm UV}=-20.5)\,[{\rm mag}^{-1}\,{\rm cMpc}^{-3}])=-4.5$, -5, and -5.2 at $z=10$ (dashed), 12 (dotted), and 16 (long dashed) from photometry. Three representative cases of different $\eta_{\rm UV}$ with fixed $\epsilon_0=0.1$ are shown by the thick vertical lines: the top-heavy models with no CHE ($f_{\rm CHE}=0$, dashed) and optimal CHE ($f_{\rm CHE}=1$, $m^{\rm CHE}_{\star,\rm min}=3\,M_\odot$, dashed–dotted) and the Salpeter model with optimal CHE ($f_{\rm CHE}=1$, $m^{\rm CHE}_{\star,\rm min}=4\,M_\odot$, dotted). The thin solid and dashed horizontal lines show the minimum and maximum UV variability estimated by X. Shen et al. (2023).

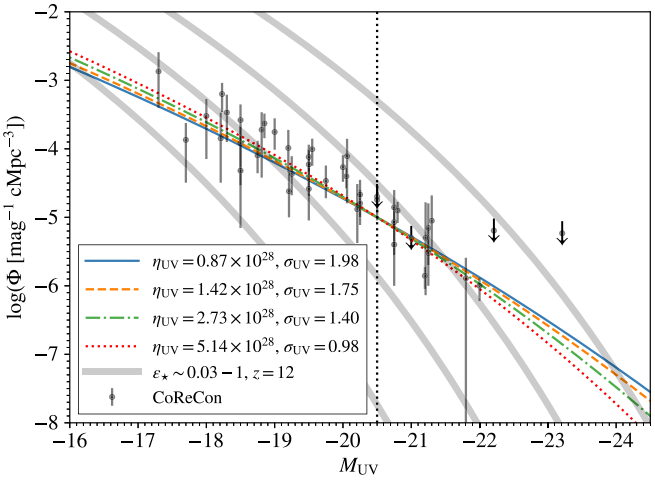

Figure 4. UVLF for select degenerate models that meet the photometric constraints from JWST at $z=12$, i.e., $\log(\Phi(M_{\rm UV}=-20.5)\,[{\rm mag}^{-1}\,{\rm cMpc}^{-3}])=-5$. These include the reference case with $\eta_{\rm UV}\simeq8.70\times10^{27}$ (solid) and the three representative models with enhanced UV emission from CHE and/or a top-heavy IMF considered in Figure 3. For comparison, the observational data for $z\sim11-13$ (R. P. Naidu et al. 2022; R. J. Bouwens et al. 2023; C. T. Donnan et al. 2023, 2024; Y. Harikane et al. 2023; P. G. Pérez-González et al. 2023; N. J. Adams et al. 2024; C. M. Casey et al. 2024; S. L. Finkelstein et al. 2024; D. J. McLeod et al. 2024; B. Robertson et al. 2024; C. J. Willott et al. 2024) are shown using CORECON (E. Garaldi 2023), among which the data points with arrows are upper limits. We also plot the results for constant SFE $\epsilon_\star=0.03$, 0.1, 0.3, and 1 (from bottom to top) without UV variability as the thick solid lines.

convolved with a Gaussian kernel of width $\sigma_{\rm UV}$ (mag) to predict the observable UVLF $\Phi\equiv dn/dM_{\rm UV}$. The last step captures the stochastic scatter in the scaling relations used above into the UV variability parameter $\sigma_{\rm UV}$.

As illustrated in X. Shen et al. (2023, see their Figure 3), the UVLFs inferred from JWST observations place constraints on $\epsilon_0\eta_{\rm UV}$ and $\sigma_{\rm UV}$, which can be estimated by considering the value of Φ at a typical magnitude $M_{\rm UV}=-20.5$. Here, we require $\log(\Phi(M_{\rm UV}=-20.5)\,[{\rm mag}^{-1}\,{\rm cMpc}^{-3}])=-5$ and -5.3 at $z=10$ and 12, according to spectroscopic observations, and $\log(\Phi(M_{\rm UV}=-20.5)\,[{\rm mag}^{-1}\,{\rm cMpc}^{-3}])=-4.5$, -5, and -5.2 at $z=10$, 12, and 16 from photometric results, using the observational data compiled by the `python` package CORECON[8] (E. Garaldi 2023). The corresponding values of $\epsilon_0\eta_{\rm UV}$ and $\sigma_{\rm UV}$ are shown in Figure 3, where larger $\epsilon_0\eta_{\rm UV}$ and/or $\sigma_{\rm UV}$ are required to explain observations at higher z, and a smaller $\epsilon_0\eta_{\rm UV}$ can be compensated with a larger $\sigma_{\rm UV}$.

To appreciate the trend and the degeneracy, we focus on three representative cases with boosted UV emission efficiency and fixed $\epsilon_0=0.1$: the top-heavy ($\alpha=1$) models with no CHE ($f_{\rm CHE}=0$) and optimal CHE ($f_{\rm CHE}=1$, $m^{\rm CHE}_{\star,\rm min}=4\,M_\odot$) and the Salpeter ($\alpha=2.35$) model with optimal CHE ($f_{\rm CHE}=1$, $m^{\rm CHE}_{\star,\rm min}=3\,M_\odot$). The corresponding UV variability parameters inferred from the photometric constraints at $z\sim12$ (16) are $\sigma_{\rm UV}=1.75$, 1.40, and 0.98 (2.55, 2.31, and 2.06), respectively, while the reference value $\eta_{\rm UV}\simeq8.70\times10^{27}$ requires $\sigma_{\rm UV}=1.98$ (2.72). Clearly, with enhanced $\eta_{\rm UV}$ from CHE, smaller (less extreme) values of ϵ_0 and $\sigma_{\rm UV}$ are required to explain JWST results. In particular, only for the Salpeter model with optimal CHE ($f_{\rm CHE}=1$, $m^{\rm CHE}_{\star,\rm min}=3\,M_\odot$, $\alpha=2.35$) the $\sigma_{\rm UV}$ needed at $z\sim16$ remains below the maximum value 2.2 estimated by X. Shen et al. (2023). Figure 4 shows the UVLFs of the (degenerate) models at $z\sim12$, which all agree well with current observations but differ slightly in shape: the evolution of Φ with $M_{\rm UV}$ is stronger for larger (smaller) $\epsilon_0\eta_{\rm UV}$ ($\sigma_{\rm UV}$), especially at the luminous end. Therefore, high-precision measurements of UVLFs (in larger survey volumes) can potentially break the degeneracy between $\epsilon_0\eta_{\rm UV}$ and $\sigma_{\rm UV}$. Additional constraints from galaxy clustering properties are also useful (J. B. Muñoz et al. 2023; G. Sun et al. 2024).

[8] https://corecon.readthedocs.io/en/latest/index.html

4. Summary and Discussion

We explore the contribution of rapidly rotating stars under CHE to the rest-frame UV ($\lambda\sim1500$ Å) emission of the first galaxies. By incorporating CHE into a simple population synthesis model under the assumptions of *blackbody spectrum* and *negligible nebular emission*, we predict the UV emission efficiency $\eta_{\rm UV}\propto L_\nu({\rm UV})/{\rm SFR}$ as a function of the mass fraction $f_{\rm CHE}$ and minimum mass $m^{\rm CHE}_{\star,\rm min}$ of CHE stars with two power-law IMF models ($dN/dm_\star\propto m_\star^{-\alpha}$, $\alpha=2.35$ and 1, $m_\star<300\,M_\odot$). We then adopt the model in X. Shen et al. (2023) to calculate the relevant UVLF.

We find that CHE can significantly enhance the rest-frame UV emission of star-forming galaxies as efficient as alternative scenarios of enhanced SFE and top-heavy IMFs. Compared with the canonical value from local calibrations (P. Madau & M. Dickinson 2014), $\eta_{\rm UV}$ is increased by a factor of $\sim3-6$ for $f_{\rm CHE}\gtrsim0.5$ and $m^{\rm CHE}_{\star,\rm min}\sim2$–$10\,M_\odot$ with a Salpeter IMF ($\alpha=2.35$) at the typical star formation timescale $t_{\rm SF}\sim100$ Myr. The effect of CHE is generally stronger for larger $t_{\rm SF}$ or IMF slope α. The enhanced UV emission from CHE can reproduce the UVLFs inferred from observations at $z\sim12-16$ with less extreme values of SFE and stochastic variability of UV luminosity, within the range of current

theoretical predictions. Taking into account nebular emission can further enhance the effect of CHE by up to a factor of $\sim$2 for $Z \gtrsim 0.0004$ (see Appendix B).

Moreover, compared with top-heavy IMFs, a potential advantage of the CHE scenario is that the enhancement of SN feedback is likely weaker, making it less vulnerable to the global suppression of star formation by such feedback (T. B. Jeong et al. 2024). We estimate the (IMF-averaged) SN energy per unit stellar mass $\mathcal{E}_{\rm SN}$ for our pure CHE and nonrotating populations using the SN models in S. Goswami et al. (2022), assuming that the SN explosion of a star undergoing CHE is identical to that of the (pre-SN) helium core with the same mass (ignoring mass loss).[9] In the metal-poor regime ($Z \lesssim 0.01$) of high-z galaxies, $\mathcal{E}_{\rm SN}$ is enhanced by a factor of $\sim$25−34 in the top-heavy ($\alpha = 1$) model of nonrotating stars compared with the canonical case of Salpeter IMF ($\alpha = 2.35$). On the other hand, in the optimal CHE model with $\alpha = 2.35$ and $m_{\star,\rm min}^{\rm CHE} = 4\,M_\odot$, $\mathcal{E}_{\rm SN}$ is only boosted by a factor of $\sim$8−11, comparable to the increase of $\eta_{\rm UV}$. This means that the effects of CHE on UV emission and SN feedback can be similar to those of increasing the SFE. However, unlike the latter, CHE is not limited by the baryon mass budget.

Besides, stellar UV spectra become harder under CHE (see also Y. Sibony et al. 2022; B. Liu et al. 2025, in preparation), which may play a role in the decrease of the UV continuum slope β (from the fit $L_\lambda \propto \lambda^\beta$ for $\lambda \sim 1270$−2600 Å) with redshift and extremely blue galaxies with $\beta \lesssim -2.6$ in observations (e.g., D. Dottorini et al. 2024). In our top-heavy (Salpeter) IMF models, for CHE stars with $m_{\star,\rm min}^{\rm CHE} = 1.7\,M_\odot$, we obtain $\beta \sim -3$ (-2.4) and -2.3 (-2) at 10 and 100 Myr after the starburst, respectively, while nonrotating stars give larger values, $\beta \sim -2.7$ (-2.2) and -1.2 (-1), under the same condition.[10]

Although this work focuses on the UV continuum, stellar and nebular lines are also affected by CHE and fast rotation in general (e.g., B. Kubátová et al. 2019; S. L. Newman et al. 2025). In addition to boosting the UV emission (as well as ionizing power, see, e.g., Y. Sibony et al. 2022; B. Liu et al. 2025, in preparation) of galaxies, populations of chemically homogeneous stars may have consequences for the nature of transients and for stellar nucleosynthesis. If homogeneous evolution is triggered by fast rotation, those stars (at least the massive ones) may produce long soft gamma-ray bursts (GRBs) via the collapsar mechanism (e.g., S. C. Yoon & N. Langer 2005; S. C. Yoon et al. 2006, 2012; M. Cantiello et al. 2007). With the extension to high redshifts considered here, GRBs may then also originate in the first galaxies (e.g., V. Bromm & A. Loeb 2006), and their associated bright afterglows could act as background sources to probe the early intergalactic medium with absorption spectroscopy (F. Y. Wang et al. 2012). The latter would be an ideal target for the upcoming suite of extremely large telescopes. CHE can play important roles in post-MS and binary stellar evolution, regulating the properties of evolved stars and binary products, such as Wolf–Rayet stars, X-ray binaries, and binary black hole mergers (e.g., J. J. Eldridge & E. R. Stanway 2012; S. C. Yoon et al. 2012; S. E. de Mink & I. Mandel 2016; I. Mandel & S. E. de Mink 2016; P. Marchant et al. 2017; B. Kubátová et al. 2019; L. du Buisson et al. 2020; J. Riley et al. 2021; H. Umeda & C. Nagele 2024; M. Dall'Amico et al. 2025). Moreover, those stars, if they lose mass, may enrich their surroundings in helium, hydrogen-burning products, and possibly also some helium-burning products, while being depleted in lithium. This material could furthermore exhibit strong carbon overabundances, thus leading to the formation of next-generation carbon-enhanced metal-poor stars (B. Liu et al. 2021; S. K. Jeena et al. 2023). All these aspects would deserve to be explored in future studies, illustrating the various manifestations of rapid rotation in the early universe.

Acknowledgments

B.L. gratefully acknowledges funding from the Deutsche Forschungsgemeinschaft (DFG; German Research Foundation) under Germany's Excellence Strategy EXC 2181/1—390900948 (the Heidelberg STRUCTURES Excellence Cluster). Y.S. and G.M. have received funding from the European Research Council (ERC) under the European Union's Horizon 2020 research and innovation program (grant agreement No. 833925, project STAREX).

Appendix A
SFR–UV Conversion Factors for Different Star Formation Timescales

Figures 5 and 6 show the results of $\eta_{\rm UV}$ for $t_{\rm SF} = 10$ and 1000 Myr, respectively, complementing the results for $t_{\rm SF} = 100$ Myr in Figure 2.

[9] We have ignored two competing effects possibly associated with CHE: the enhancement of SN energy by fast rotation (e.g., A. Burrows et al. 2007; A. Maeder & G. Meynet 2012; K.-J. Chen 2015; S. Fujibayashi et al. 2023) and the reduction of core mass by strong Wolf–Rayet-like winds during post-MS or near the end of MS (e.g., S. C. Yoon et al. 2012; B. Kubátová et al. 2019; J. Riley et al. 2021; H. Umeda & C. Nagele 2024). Taking them into account in a detailed investigation of the SN feedback from CHE stars is deferred to future work.

[10] Note that these results do not consider nebular emission and treat stars as blackbodies. According to the TLUSTY stellar atmosphere models, the spectral shape of UV continuum at $\lambda \sim 1270$−2600 Å does not deviate much from that of blackbodies for hot stars. Besides, the nebular contributions can be small in extremely blue galaxies due to high escape fractions and/or bursty star formation (D. Dottorini et al. 2024).

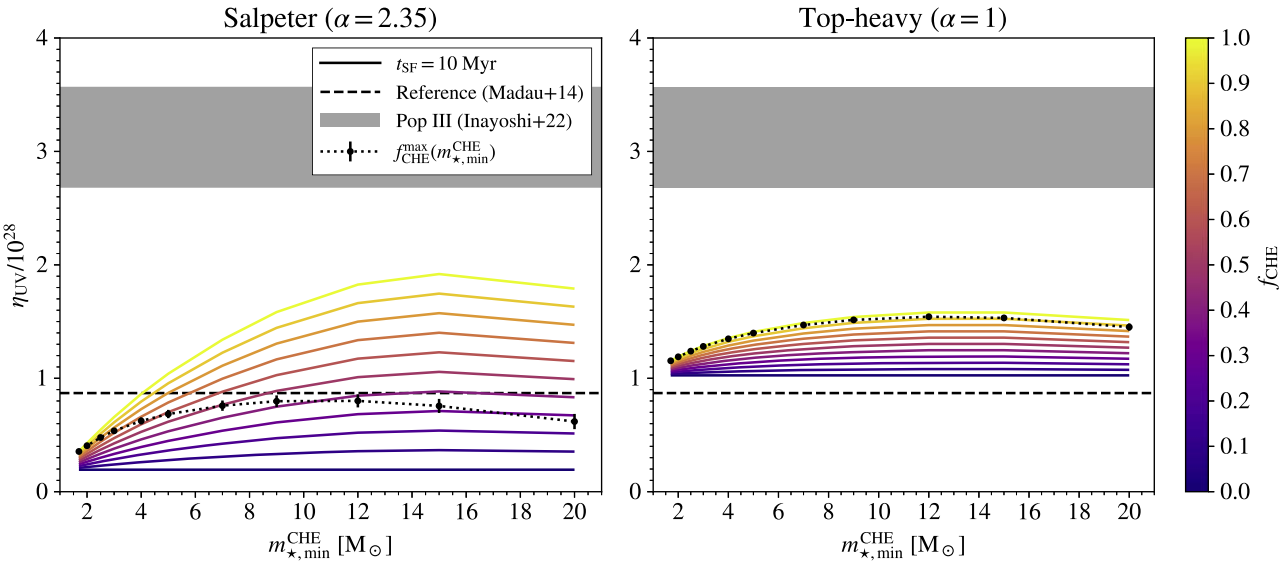

Figure 5. Same as Figure 2 but for a star formation timescale $t_{\rm SF} = 10$ Myr.

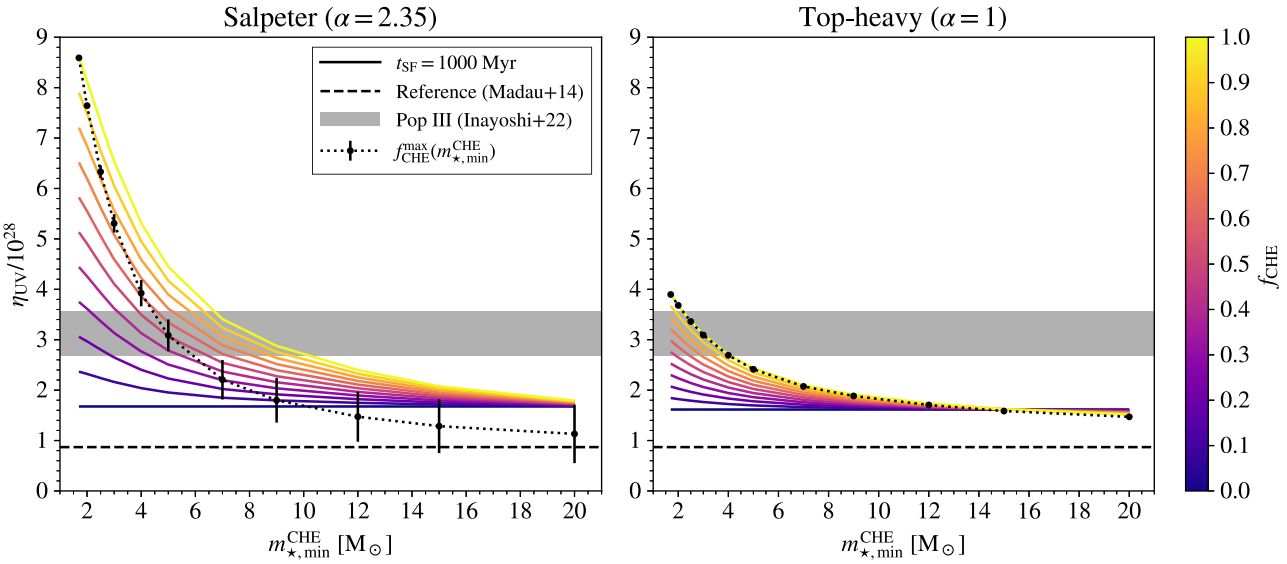

Figure 6. Same as Figure 2 but for a star formation timescale $t_{\rm SF} = 1000$ Myr.

Appendix B
Contribution of Nebular Emission

We use the Yggdrasil models (E. Zackrisson et al. 2011) to estimate the possible contribution of nebular emission in rest-frame UV. As shown in Figure 7, nebular emission is strongest for very young star-forming clouds, reaching up to $\sim$40% of the stellar luminosity in moderately metal-enriched environments with $Z \geqslant 0.0004$. However, it decays with time and becomes negligible ($\lesssim$10% of the stellar contribution) shortly ($\sim$ a few Myr $\ll t_{\rm SF}$) after the starburst. Besides, for continuous star formation with a constant SFR over the past $t_{\rm SF} = 100(10)$ Myr, the nebular luminosity is below 10(20)% of the stellar luminosity. Note that E. Zackrisson et al. (2011) only consider nonrotating stars without CHE and adopt a P. Kroupa (2001) IMF in the mass range $m_\star \in [0.1, 100]\,M_\odot$ for $Z \geqslant 0.0004$. The nebular emission is stronger at lower metallicities and when the stellar ionizing radiation is enhanced. In the Yggdrasil models of metal-free clouds hosting nonrotating Pop III stars, nebular emission can dominate the rest-frame UV luminosity in the first few Myr and remain comparable to stellar emission for up to $\sim$20 Myr after a starburst or continuous star formation with $t_{\rm SF} \sim 10-100$ Myr. Here, the nebular contribution is approximately proportional to the stellar ionizing flux. If this trend holds for moderately metal-enriched ($Z \gtrsim 0.0004$) galaxies most relevant for JWST observations, nebular emission can become comparable to stellar emission in rest-frame UV under CHE, since the production of ionizing photons is boosted by up to a factor of a few by CHE (Y. Sibony et al. 2022; B. Liu et al. 2025, in preparation).

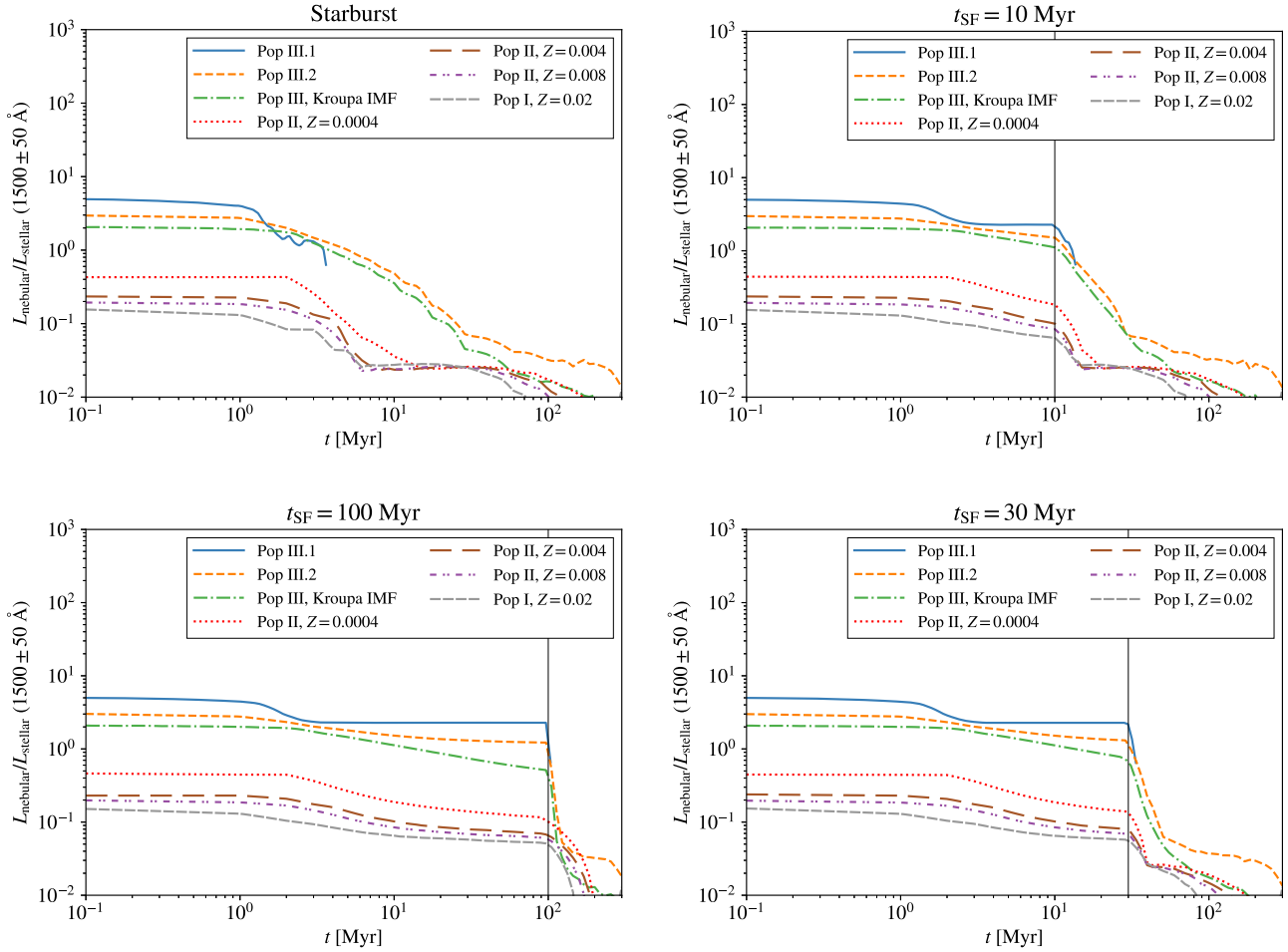

Figure 7. Ratio between nebular and stellar luminosities in rest-frame UV (1500 ± 50 Å) from an instantaneous starburst and continuous star formation (starting at $t = 0$) with a constant rate over timescales $t_{\rm SF} = 10$, 30, and 100 Myr (clockwise) for the Yggdrasil models (E. Zackrisson et al. 2011), assuming no leakage of ionizing photons (optimistic nebular emission). Among these are two models for Pop III stars with top-heavy IMFs: a Salpeter-like power law ($dN/dm_\star \propto m_\star^{-2.35}$) in the range $m_\star \in [50, 500]\,M_\odot$ (Pop III.1, solid) and a log-normal distribution with characteristic mass $m_{\star,\rm c} = 10\,M_\odot$ and dispersion (in $\ln m_\star$) $\sigma = 1$ for $m_\star \in [1, 500]\,M_\odot$ (Pop III.2, dashed), one Pop III model with a P. Kroupa (2001) IMF in $m_\star \in [0.1, 100]\,M_\odot$ (dashed–dotted), three Pop II models with the same P. Kroupa (2001) IMF and different metallicities: $Z = 0.0004$ (dotted), 0.004 (long dashed), 0.008 (dashed–dotted-dotted), and a Pop I (densely dashed) model with the same P. Kroupa (2001) IMF and $Z = 0.02$. For the cases with continuous star formation, we are mainly interested in the results at $t = t_{\rm SF}$ (labeled with vertical lines), which denotes the moment of observation, i.e., when the galaxy has been forming stars for a duration of $t_{\rm SF}$.

ORCID iDs

Boyuan Liu https://orcid.org/0000-0002-4966-7450
Yves Sibony https://orcid.org/0000-0002-7829-776X
Georges Meynet https://orcid.org/0000-0001-6181-1323
Volker Bromm https://orcid.org/0000-0003-0212-2979

References

Adams, N. J., Conselice, C. J., Austin, D., et al. 2024, ApJ, 965, 169
Aguilera-Dena, D. R., Langer, N., Moriya, T. J., & Schootemeijer, A. 2018, ApJ, 858, 115
Anglés-Alcázar, D., Faucher-Giguère, C.-A., Kereš, D., et al. 2017, MNRAS, 470, 4698
Behroozi, P., Wechsler, R. H., Hearin, A. P., & Conroy, C. 2019, MNRAS, 488, 3143
Benz, W., & Hills, J. G. 1987, ApJ, 323, 614
Bouwens, R. J., Stefanon, M., Brammer, G., et al. 2023, MNRAS, 523, 1036
Boylan-Kolchin, M. 2023, NatAs, 7, 731
Bromm, V., Kudritzki, R. P., & Loeb, A. 2001, ApJ, 552, 464
Bromm, V., & Loeb, A. 2006, ApJ, 642, 382
Brott, I., de Mink, S. E., Cantiello, M., et al. 2011, A&A, 530, A115
Bunker, A. J., Saxena, A., Cameron, A. J., et al. 2023, A&A, 677, A88
Burrows, A., Dessart, L., Livne, E., Ott, C. D., & Murphy, J. 2007, ApJ, 664, 416
Cantiello, M., Yoon, S. C., Langer, N., & Livio, M. 2007, A&A, 465, L29
Casey, C. M., Akins, H. B., Shuntov, M., et al. 2024, ApJ, 965, 98
Chen, K.-J. 2015, MPLA, 30, 1530002
Cueto, E. R., Hutter, A., Dayal, P., et al. 2024, A&A, 686, A138
Cui, Z., Wang, Z., Zhu, C., et al. 2018, PASP, 130, 084202
Dall'Amico, M., Mapelli, M., & Giuliano, I. 2025, arXiv:2501.04778
de Mink, S. E., & Mandel, I. 2016, MNRAS, 460, 3545
Dekel, A., Sarkar, K. C., Birnboim, Y., Mandelker, N., & Li, Z. 2023, MNRAS, 523, 3201
D'Eugenio, F., Maiolino, R., Carniani, S., et al. 2024, A&A, 689, A152
Donnan, C. T., Dunlop, J. S., McLure, R. J., McLeod, D. J., & Cullen, F. 2025, arXiv:2501.03217
Donnan, C. T., McLeod, D. J., McLure, R. J., et al. 2023, MNRAS, 520, 4554
Donnan, C. T., McLure, R. J., Dunlop, J. S., et al. 2024, MNRAS, 533, 3222
Dorozsmai, A., Toonen, S., Vigna-Gómez, A., de Mink, S. E., & Kummer, F. 2024, MNRAS, 527, 9782
Dottorini, D., Calabrò, A., Pentericci, L., et al. 2024, arXiv:2412.01623
du Buisson, L., Marchant, P., Podsiadlowski, P., et al. 2020, MNRAS, 499, 5941
Eldridge, J. J., Langer, N., & Tout, C. A. 2011, MNRAS, 414, 3501
Eldridge, J. J., & Stanway, E. R. 2012, MNRAS, 419, 479
Eldridge, J. J., & Stanway, E. R. 2016, MNRAS, 462, 3302
Fakhouri, O., Ma, C.-P., & Boylan-Kolchin, M. 2010, MNRAS, 406, 2267

Ferrara, A. 2024, A&A, 689, A310
Finkelstein, S. L., Bagley, M. B., Ferguson, H. C., et al. 2023, ApJL, 946, L13
Finkelstein, S. L., Leung, G. C. K., Bagley, M. B., et al. 2024, ApJL, 969, L2
Flores Velázquez, J. A., Gurvich, A. B., Faucher-Giguère, C.-A., et al. 2021, MNRAS, 501, 4812
Fujibayashi, S., Sekiguchi, Y., Shibata, M., & Wanajo, S. 2023, ApJ, 956, 100
Garaldi, E. 2023, JOSS, 8, 5407
Ghodla, S., Eldridge, J. J., Stanway, E. R., & Stevance, H. F. 2023, MNRAS, 518, 860
Gormaz-Matamala, A. C., Cuadra, J., Ekström, S., et al. 2024, A&A, 687, A290
Goswami, S., Silva, L., Bressan, A., et al. 2022, A&A, 663, A1
Hainich, R., Pasemann, D., Todt, H., et al. 2015, A&A, 581, A21
Harikane, Y., Ouchi, M., Oguri, M., et al. 2023, ApJS, 265, 5
Hirano, S., & Bromm, V. 2018, MNRAS, 476, 3964
Hubeny, I. 1988, CoPhC, 52, 103
Hubeny, I., Allende Prieto, C., Osorio, Y., & Lanz, T. 2021, arXiv:2104.02829
Inayoshi, K., Harikane, Y., Inoue, A. K., Li, W., & Ho, L. C. 2022, ApJL, 938, L10
Iorio, G., Mapelli, M., Costa, G., et al. 2023, MNRAS, 524, 426
Jeena, S. K., Banerjee, P., Chiaki, G., & Heger, A. 2023, MNRAS, 526, 4467
Jeong, T. B., Jeon, M., Song, H., & Bromm, V. 2024, ApJ, 980, 10
Katz, H., Ji, A. P., Telford, G., & Senchyna, P. 2024, OJAp, 7, 106
Kroupa, P. 2001, MNRAS, 322, 231
Kubátová, B., Szécsi, D., Sander, A. A. C., et al. 2019, A&A, 623, A8
Labbé, I., van Dokkum, P., Nelson, E., et al. 2023, Natur, 616, 266
Liu, B., & Bromm, V. 2022, ApJL, 937, L30
Liu, B., Gurian, J., Inayoshi, K., et al. 2024, MNRAS, 534, 290
Liu, B., Sibony, Y., Meynet, G., & Bromm, V. 2021, MNRAS, 506, 5247
Madau, P., & Dickinson, M. 2014, ARA&A, 52, 415
Maeder, A. 1987, A&A, 178, 159
Maeder, A., & Meynet, G. 2000, ARA&A, 38, 143
Maeder, A., & Meynet, G. 2012, RvMP, 84, 25
Mandel, I., & de Mink, S. E. 2016, MNRAS, 458, 2634
Marchant, P., Langer, N., Podsiadlowski, P., et al. 2017, A&A, 604, A55
McLeod, D. J., Donnan, C. T., McLure, R. J., et al. 2024, MNRAS, 527, 5004
Muñoz, J. B., Mirocha, J., Furlanetto, S., & Sabti, N. 2023, MNRAS, 526, L47
Murphy, L. J., Groh, J. H., Ekström, S., et al. 2021, MNRAS, 501, 2745
Murray, S. G., Power, C., & Robotham, A. S. G. 2013, A&C, 3, 23
Naidu, R. P., Oesch, P. A., van Dokkum, P., et al. 2022, ApJL, 940, L14
Nandal, D., Sibony, Y., & Tsiatsiou, S. 2024, A&A, 688, A142
Newman, S. L., Lovell, C. C., Maraston, C., et al. 2025, arXiv:2501.03133
Pérez-González, P. G., Costantin, L., Langeroodi, D., et al. 2023, ApJL, 951, L1
Planck Collaboration, Aghanim, N., Akrami, Y., et al. 2020, A&A, 641, A6
Riley, J., Mandel, I., Marchant, P., et al. 2021, MNRAS, 505, 663
Robertson, B., Johnson, B. D., Tacchella, S., et al. 2024, ApJ, 970, 31
Salpeter, E. E. 1955, ApJ, 121, 161
Sander, A., Shenar, T., Hainich, R., et al. 2015, A&A, 577, A13
Sander, A. A. C., Fürst, F., Kretschmar, P., et al. 2018, A&A, 610, A60
Sander, A. A. C., Hamann, W. R., Todt, H., Hainich, R., & Shenar, T. 2017, A&A, 603, A86
Shen, X., Vogelsberger, M., Boylan-Kolchin, M., Tacchella, S., & Kannan, R. 2023, MNRAS, 525, 3254
Shen, X., Vogelsberger, M., Boylan-Kolchin, M., Tacchella, S., & Naidu, R. P. 2024, MNRAS, 533, 3923
Sibony, Y., Liu, B., Simmonds, C., Meynet, G., & Bromm, V. 2022, A&A, 666, A199
Song, H. F., Meynet, G., Maeder, A., Ekström, S., & Eggenberger, P. 2016, A&A, 585, A120
Stacy, A., Bromm, V., & Loeb, A. 2011, MNRAS, 413, 543
Stacy, A., Greif, T. H., Klessen, R. S., Bromm, V., & Loeb, A. 2013, MNRAS, 431, 1470
Sun, G., Muñoz, J. B., Mirocha, J., & Faucher-Giguère, C.-A. 2024, arXiv:2410.21409
Szécsi, D., Agrawal, P., Wünsch, R., & Langer, N. 2022, A&A, 658, A125
Szécsi, D., Langer, N., Yoon, S.-C., et al. 2015, A&A, 581, A15
Tacchella, S., Bose, S., Conroy, C., Eisenstein, D. J., & Johnson, B. D. 2018, ApJ, 868, 92
Tacchella, S., Forbes, J. C., & Caplar, N. 2020, MNRAS, 497, 698
Telford, O. G., Chisholm, J., Sander, A. A. C., et al. 2024, ApJ, 974, 85
Tinker, J. L., Robertson, B. E., Kravtsov, A. V., et al. 2010, ApJ, 724, 878
Topping, M. W., Stark, D. P., Senchyna, P., et al. 2024, MNRAS, 529, 3301
Trinca, A., Schneider, R., Valiante, R., et al. 2024, MNRAS, 529, 3563
Tsiatsiou, S., Sibony, Y., Nandal, D., et al. 2024, A&A, 687, A307
Umeda, H., & Nagele, C. 2024, ApJ, 961, 146
Ventura, E. M., Qin, Y., Balu, S., & Wyithe, J. S. B. 2024, MNRAS, 529, 628
Vink, J. S., de Koter, A., & Lamers, H. J. G. L. M. 2001, A&A, 369, 574
Wang, F. Y., Bromm, V., Greif, T. H., et al. 2012, ApJ, 760, 27
Willott, C. J., Desprez, G., Asada, Y., et al. 2024, ApJ, 966, 74
Yoon, S. C., Dierks, A., & Langer, N. 2012, A&A, 542, A113
Yoon, S. C., & Langer, N. 2005, A&A, 443, 643
Yoon, S. C., Langer, N., & Norman, C. 2006, A&A, 460, 199
Zackrisson, E., Rydberg, C.-E., Schaerer, D., Östlin, G., & Tuli, M. 2011, ApJ, 740, 13
Zepeda, J., Beers, T. C., Placco, V. M., et al. 2023, ApJ, 947, 23